CHAPTER 3
Using SAR Data for Mapping Deforestation and Forest Degradation

Josef Kellndorfer, President and Senior Scientist, Earth Big Data, LLC

ABSTRACT

This chapter focuses on Synthetic Aperture Radar (SAR) observations of forest cover change from deforestation and forest degradation. Discussed are SAR backscatter changes determined by sensor and target parameters. Sensor parameters include the wavelength/frequency of the SAR, as well as incidence angle, look directions, and transmit and receive polarization. Since sensor parameters are typically stable from a satellite SAR, backscatter variations over time can be attributed to two main target parameters: structure and moisture. For forests and other targets, this means observations of backscatter change can be linked directly to change in forest structure and moisture conditions of the vegetation and underlying soil. This makes observations with SAR complementary to optical data as (1) almost no atmospheric or Sun illumination variations play a role in SAR response, and (2) longer wavelengths and active penetration into forest canopies interact directly with structure and moisture conditions.

This chapter discusses the influence of sensor and target parameters on backscatter variations from forests and a time series analysis approach for forest change detection. Also discussed are proper methods for SAR data calibration for forest applications, including preprocessing and proper data scaling. Most image examples in this chapter stem from a time series stack of Sentinel-1 data acquired over Ecuador in the Universal Transverse Mercator (UTM) projection tile of the Military Grid Reference System (MGRS), tile number 18MTE (see Fig. 3.1). (The MGRS provides a global tiling scheme with UTM zone number, row designator, and two-letter tile identifier, i.e., 18MTE = Zone 18, Row M, Tile TE. More information may be found here.) The tile is transected by the Napo and Coca rivers on the eastern slopes of the Andes.

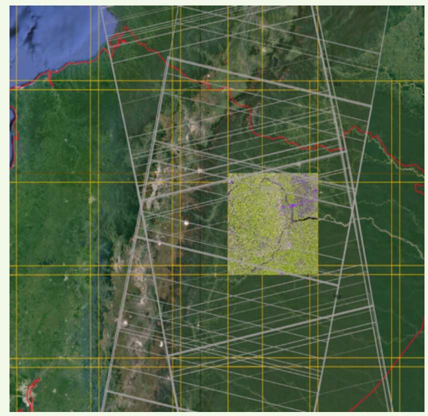

Figure 3.1 *Location of the example Military Grid Reference System (MGRS) tile 18MTE in Ecuador used in this chapter.*

3.1 SAR for Mapping Deforestation and Forest Degradation

As a vital natural resource, forests provide a host of ecosystem services, including carbon sequestration, diverse natural habitats for flora and fauna, and they are a key source of food and fiber for human consumption. Today, many nations have entered international or regional agreements (e.g., the United Nations' Framework Convention of Climate Change - Reducing Emissions from Deforestation or Forest Degradation (UNFCCC-REDD+)) to protect their forest resources. Tracking deforestation rates annually and developing early warning systems of forest loss (often from illegal activities) are essential. Remote sensing of forest change has an important role in this monitoring effort. While optical data have long been the workhorse for forest monitoring, the advent of operational SAR data availability offers an invaluable complement with a crucial sensitivity: microwave remote sensors are largely cloud-penetrating and thus guarantee continuous monitoring, even under cloudy skies. For tropical nations, this is particularly important as continuous cloud cover severely limits the availability of optical data at medium resolution (Kellndorfer et al. 2014, Mitchell et al. 2017).

3.2 Brief Review of Color Theory for Interpreting SAR Images

SAR backscatter images are representations of the microwave portion of the electromagnetic spectrum, and as such always represent grayscale or false color combinations mapped to the human visual color space. This is analogous to the false color representation of multispectral optical remote sensing imagery from bands outside the visual spectrum. (Please note that in this chapter, "SAR image" shall refer to a grayscale or multi-band image of SAR backscatter, calibrated to γ^0 with a Radiometric Terrain Correction (RTC) approach (see **Chapter 2**)).

3.2.1 GRAYSCALE DISPLAY OF SAR IMAGERY

A single-band SAR image (i.e., from one frequency and one polarization) is displayed such that low backscatter values correspond to dark colors and high backscatter values correspond to bright colors. Enhancements can be applied, like linear or histogram stretches. Examples of SAR backscatter images from Sentinel-1 are shown in **Figure 3.2** for a landscape scale subset in Ecuador and in **Figure 3.3** for a large oil palm plantation just to the north of Puerto Francisco.

3.2.2 COLOR DISPLAY OF SAR IMAGERY

For the interpretation of SAR imagery, it is useful to briefly review the basics of how multichannel SAR imagery is displayed. **Tables 3.1 and 3.2** may be used as resources for understanding colors when displaying false color SAR Images (see Henderson & Lewis 1998).

Img Layer 1 Blue	*Img Layer 2* Green	*Img Layer 3* Red	*Resultant* Color
	Tonal Change on Image		
White	Black	Black	Blue
Black	White	Black	Green
Black	Black	White	Red
White	White	Black	Cyan
White	Black	White	Magenta
Black	White	White	Yellow
	No Tonal Change on Image		
White	White	White	White
Black	Black	Black	Black
Grey	Grey	Grey	Grey

Table 3.1 *Color assignments and resultant colors for multi-dimensional SAR image composites (Manual of Remote Sensing, Vol. 2, 1998).*

Type of Composite	*Assigned Color*		
	BLUE	GREEN	RED
Multifrequency/band	Shortest λ	Middle λ	Longest λ
Multitemporal (date)	First (earliest)	Second	Third (Latest)
Multipolarized	Most to Least Common (HH)	(HV/VH)	(VV)

Table 3.2 *Often-used color scheme for multi-dimensional false color SAR composites (Manual of Remote Sensing, Vol. 2, 1998).*

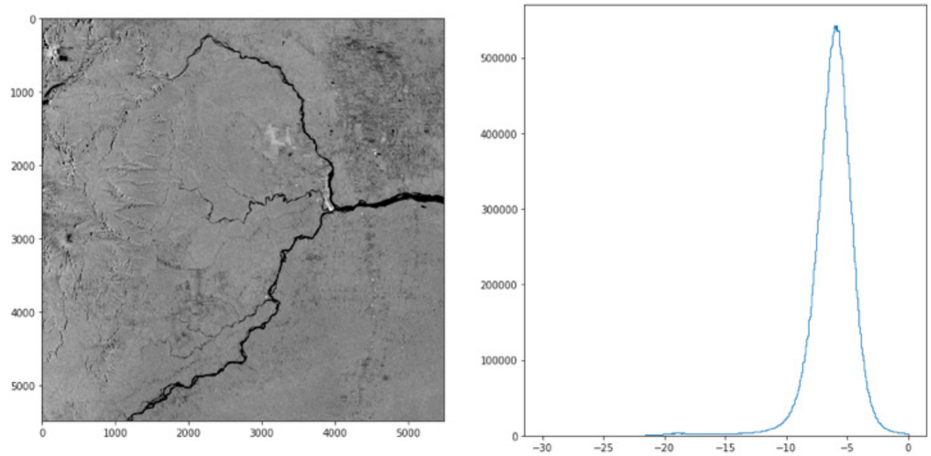

Figure 3.2 *Grayscale Sentinel-1 amplitude image in Ecuador. The area is mostly forested, with the Coca and Napo Rivers, Puerto Francisco, and an oil palm plantation being dark and bright prominent features. The Andes touch the western part of this image. The backscatter histogram in the right panel contains values ranging from about –23 to 0 dB, peaking at about –6 dB.*

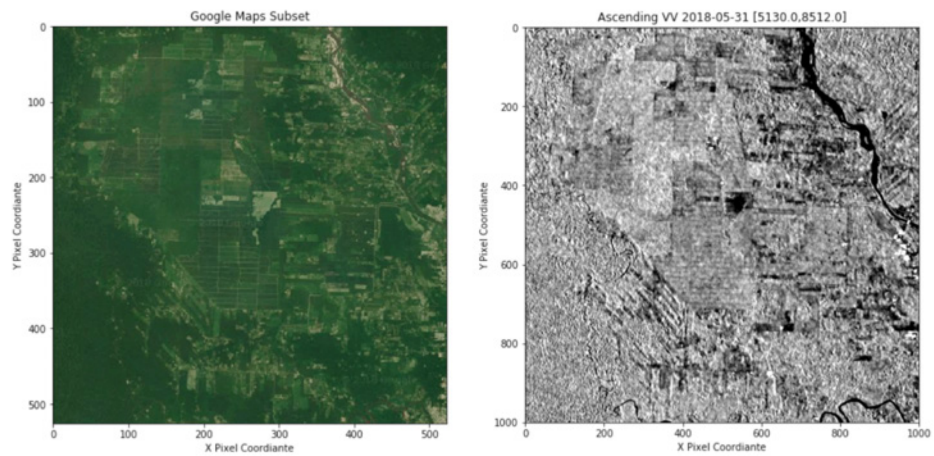

Figure 3.3 *Google Earth and Sentinel-1 images of a subset of the large oil palm plantation. While the river and most agricultural fields exhibit dark colors, the various states of regrowth in the oil palm plantation correspond to different gray values.*

Table 3.1 describes how the combination of grayscale imagery assigned to the Red/Green/Blue (RGB) bands would lead to the resulting colors when the extreme dark (black) and bright (white) colors are combined. This is useful when interpreting an RGB multitemporal color image. For example, assume that three dates are combined as per **Table 3.2**, with the earliest acquisition in red, the second acquisition in green, and the newest acquisition in blue. If a red color is seen for a pixel, according to **Table 3.1**, the red layer is close to white (bright backscatter), while the subsequent acquisitions are close to black (dark backscatter). Thus, the backscatter drops after the first acquisition, which is often a sign of deforestation or a degradation event. Note that for forest applications in particular, it is always useful to assign cross-polarized data, which are more related to volume scattering of the canopies to the green band. Co-polarized data (VV or HH) are suited for the red band, where surface scattering components are more pronounced. When only dual-polarimetric data are available (e.g., L-HH/HV from ALOS, or C-VV/VH from Sentinel-1), a color SAR image is often constructed by assigning the ratio of co-polarized to cross-polarized data to the blue channel. Note that for multi-polarized images with only two polarizations, the co-polarized band is often assigned to red, the cross-polarized to green, and the ratio of co-/cross-polarized data to the blue channel.

Examples for Sentinel-1 C-band and ALOS-1 L-band data are shown in **Figures 3.4 and 3.5**, respectively. The images show the Napo river in the southeast, an oil palm plantation in the northeast, primary rainforest in the northwest, and active fish-bone logging patterns in the southwest. The color composites are constructed from dual-polarimetric data with co-polarized data assigned to the red channel, cross-polarized data to the green channel, and the co-/cross-polarized ratio to the blue channel. A nice effect for forest applications with this color assignment strategy is that forests tend to be shown in shades of green, and typically the brightness of green corresponds to the amount of biomass in the forest. Also, water tends to be represented in blue colors, which also represent other surface scattering components. Naturally, different histogram stretches may be applied to enhance various surface components. In these examples, it is remarkable that both C-VV/VH and L-HH/HV false color SAR composites over this predominantly forested landscape exhibit similar color impressions. Differences are notable, however, foremost by the appearance of some dark green color in agricultural areas in the C-band composite. This likely stems from higher sensitivity to volume scattering from agricultural crops, which have less of a volume scattering component at L-band.

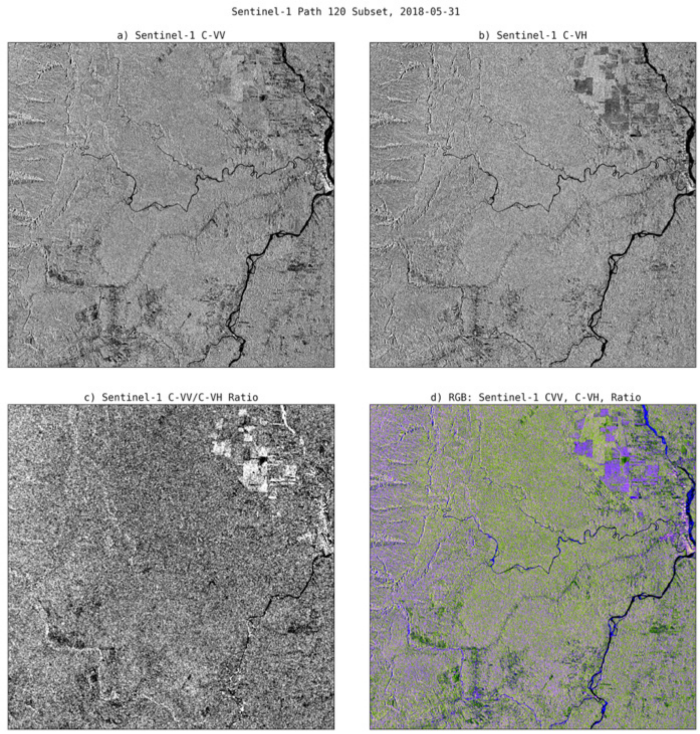

Figure 3.4 *Sentinel-1 C-band dual polarimetric VV and VH data: (a) VV, (b) VH, (c) VV/VH ratio, and (d) SAR false color composite with RGB = VV/VH/ratio channel assignment. Image acquired on May 31, 2018.*

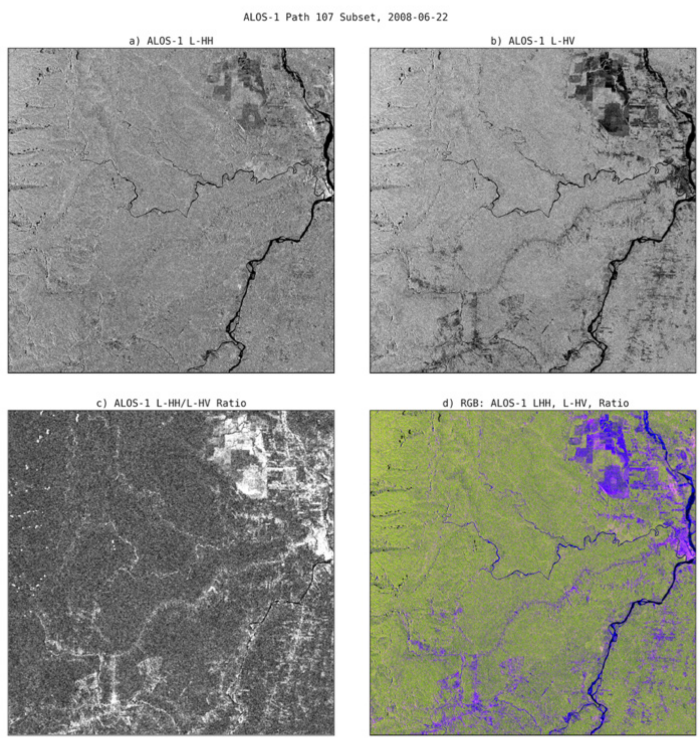

Figure 3.5 *ALOS-1 L-band dual-polarimetric HH and HV data: (a) HH, (b) HV, (c) HH/HV ratio, and (d) SAR false color composite with RGB = HH/HV/ratio channel assignment. Same area as in* ***Figure 3.4****, acquired ~10 years earlier on June 22, 2008.*

3.3 Review of SAR Characteristics for Forest Mapping

SAR backscatter values are determined by two main groups of characteristics: sensor and target characteristics. The first group includes the frequency/wavelength of the SAR, polarization of the transmitted and received SAR signal, incidence angle of the radar beam interacting with the ground, and look direction of the sensor. The combination of these characteristics needs to be considered when interpreting and analyzing SAR imagery. It is often ill-advised to combine SAR imagery from a set of varying sensor parameters if the backscatter data are not carefully cross-calibrated. For time series analysis in particular, it is advisable to analyze data from the same sensor characteristics, otherwise signal variations can be misinterpreted as true change, though no change has actually occurred. The following sections review with examples the main sensor characteristics to point to these differences.

The other group of characteristics determining SAR backscatter of forests and other natural and manmade targets are related to target characteristics. In general, assuming constant imaging sensor characteristics, SAR backscatter is a function of a target's moisture content and structural characteristics. For forests, this means that forest volume (biomass) and structural complexity (forest trunks, branches, and leaves) can indicate species present (e.g., pines vs. deciduous). Unlike optical imagery, if sensor parameters are stable—as is the case with most repeat-pass orbiting SAR sensors—signal variations at any given pixel location are only a function of these target characteristics. Sun angle variations seen in optical data do not affect the active SAR sensing system. Also, atmospheric variations (including clouds) have (almost) no impact on the SAR signal; however, there are notable and important exceptions at shorter wavelength SARs when heavy active rain events are encountered, as seen in C-band observations over tropical environments. Thus, when analyzing radar signals, it is important to recognize that moisture changes in both soil and vegetation strongly determine SAR backscatter. For some key concepts in understanding SAR backscatter from forests and natural vegetation, see Ulaby et al. 1986, 1989, 1990, 2014; Henderson & Lewis 1998; Woodhouse 2006; and Kellndorfer & McDonald 2008.

3.3.1 ROLE OF FREQUENCY IN FORESTS

SAR frequency determines the wavelength of the electromagnetic wave interacting with targets such as forests. In a nutshell, the longer the wavelength (i.e., the smaller the frequency), the more a wave penetrates into forest canopies and interacts with larger parts of the forest volume. In a simplistic view, one can attribute X-band (at about 3 cm) to mostly crown and small branch and leaf/needle scattering. C-band (5 cm) penetrates somewhat deeper into crowns and scatters on medium-sized branches. L-band (23 cm) and P-band (40 cm) have strongest penetration capacity and interact with larger parts of trees like big branches and trunks (see **Chapter 2, Fig. 2.6**). As such, L-band and longer wavelengths are often connected with a strong "double-bounce" scattering component, where the incident energy is scattered forward towards the ground where it bounces back to the sensor (similar to a racquetball or squash). This double-bounce effect is invaluable for detecting below-canopy flooding effects where inundation with standing water below a tree acts as a strong reflecting surface in the forward direction back to the SAR instrument. In tropical forest environments, riparian forests are thus extremely bright in SAR imagery when flooded (**Fig. 3.6**).

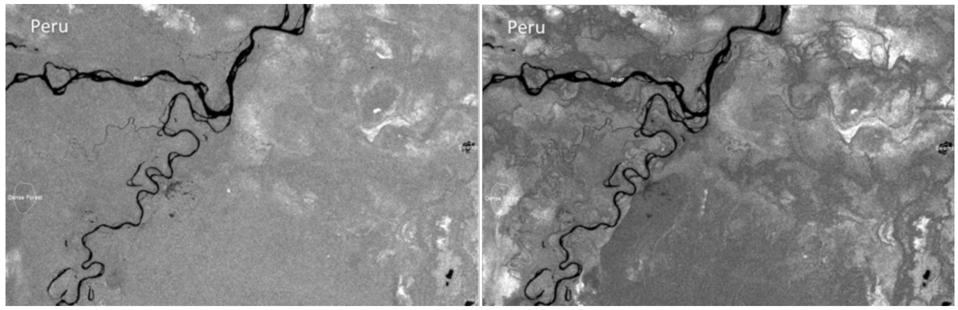

Figure 3.6 *Double-bounce effect from bellow-canopy flooding at L-HH polarization from ALOS-1: (a) Low-water season and (b) high-water season. Note the brightening of the forests during inundation.*

Figures 3.7 and 3.8 show L- and C-band backscatter images of the oil palm plantation in Ecuador. Although the C-band data are from a timeframe of 10 years after the L-band acquisitions, most notably, the relative absence of very dark surfaces in the C-band data points to strong backscatter from rough surfaces at the shorter wavelengths, whereas at the L-band, surfaces appear smoother (hence, darker) when little or no vegetation is present.

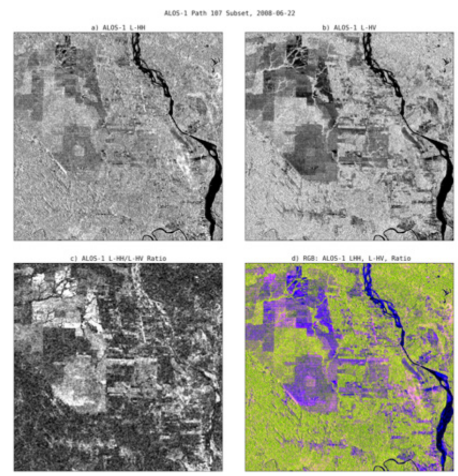

Figure 3.7 *ALOS-1 L-band imagery for the oil palm plantation: (a) L-HH, (b) L-HV, (c) ratio, and (d) RGB composite LHH/LHV/ratio.*

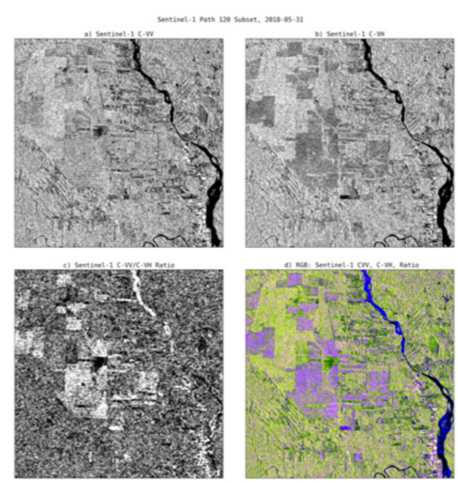

Figure 3.8 *Sentinel-1 C-band imagery for the oil palm plantation: (a) C-VV, (b) C-VH, (c) ratio, and (d) RGB composite CVV/CVH/ratio.*

3.3.2 ROLE OF POLARIZATION IN FORESTS

It is important to consider the polarization of radar waves interacting with forests, as it determines how the signal interacts with trunks and crown components. **Figure 3.9** shows a simplified diagram of how long and short wavelengths at horizontal and vertical polarizations interact with forests. Most important is that backscatter from co-polarization (VV, HH) (i.e., same transmit and receive components) is typically stronger for surface scattering components, whereas energy measured from cross-polarized (VH or HV) detection (i.e., measuring energy returning at a 90° offset to the transmitting wave) is associated with measuring volume scattering. **Chapter 2, Section 2.2.3** provides a good background about polarization and sur-

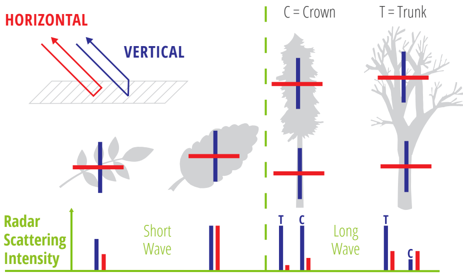

Figure 3.9 *Schematic effects of polarization on backscatter of long and short wavelengths scattering from trunks and crowns.*

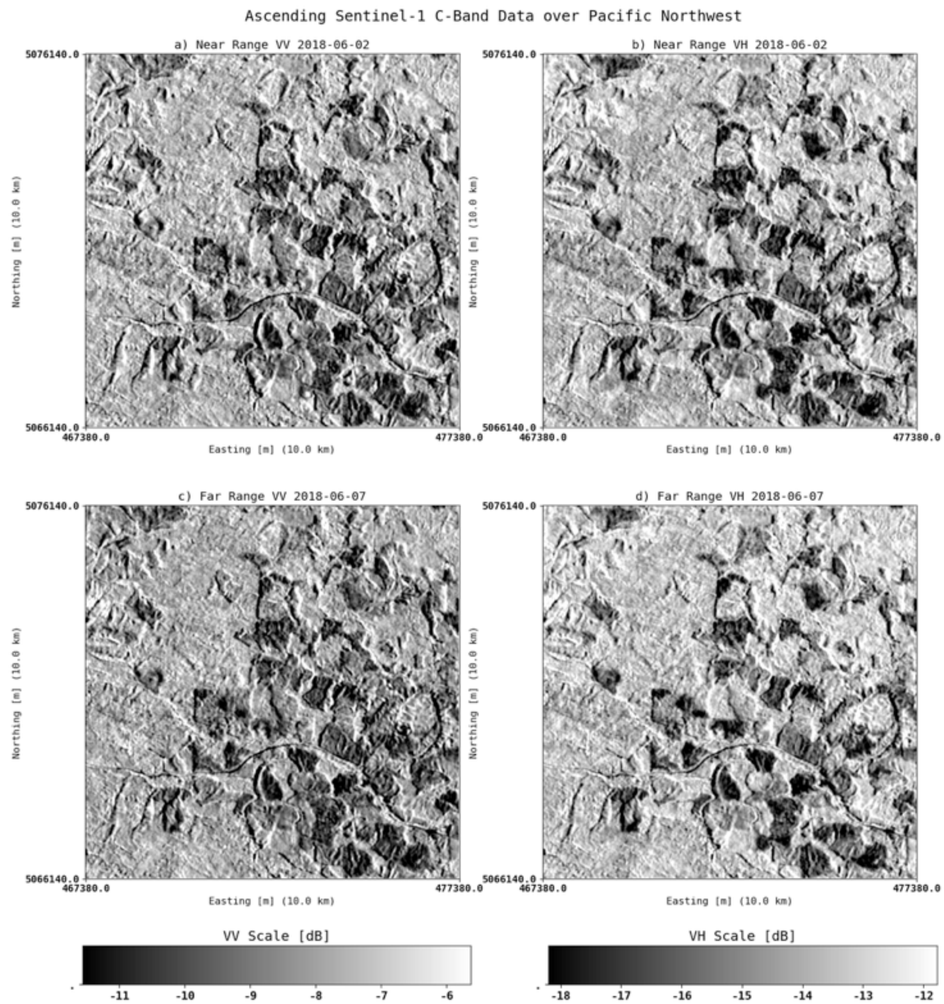

Figure 3.10 *Near- and far-range acquisitions of Sentinel-1 CVV and CVH data over a forested site in the Pacific Northwest.*

face scattering types. Thus, for biomass applications, forest degradation tracking, and identifying changes from volumes to surfaces, cross-polarized observations with SAR imagery are essential. The differences between like and cross-polarized imagery from the C- and L-bands of the oil palm plantation are visible in **Figures 3.7 and 3.8**. It can clearly be seen at both L-HH or C-VV that large gray value ambiguities exist between forest canopies and non-forest regions. In the cross-polarized images, these distinctions are more readily made and less ambiguous. Note for example in the L-band image's lower part in **Figure 3.5** that the fishbone logging pattern visible in the HV polarization is not visible in the HH polarization.

3.3.3 ROLE OF INCIDENCE ANGLE

The incidence angle describes the angle between the sensor and ground and the surface normal of the illuminated surface (see **Chapter 2**). SAR backscatter is strongly influenced by this angle, as it determines scattering in the crown layer, trunks, and interactions with the ground. If slopes are tilted toward the sensor, stronger backscatter can be expected. If slopes are tilted away from the sensor, weaker backscatter is to be expected. RTC will account for these effects to some degree; however, scattering behavior is strongly dependent on the type of surface cover. This effect is weaker over dense forested environments and stronger over sparse vegetation or bare soils.

Figure 3.10 is an example from the Pacific Northwest of the United States where timber management involves clearcutting, selective logging, and replanting. The Sentinel-1 images show acquisitions in the subset from overlapping paths, one imaging the area closer to near range (steeper incidence angle) of the SAR sensor and one closer to far range (shallower incidence angle) of the sensor. While not immediately obvious, close inspection of the figure shows differences in the near- and far-range acquisitions only five days apart where no significant rain events have changed moisture conditions. The rows show near- and far-range data for VV and VH data in the columns. A comparison of the top and bottom figures in each column illustrates the differences stemming from variations in incidence angles from the overlapping paths.

3.3.4 ROLE OF LOOK DIRECTION (ASCENDING/DESCENDING) DATA TAKES

The look direction of a SAR refers to the direction the radar antenna is pointed when emitting and receiving the radar beam. A SAR look direction is determined with respect to the flight direction of the sensor (see **Chapter 2, Sec. 2.1**). It is analogous to sitting on the right or left side of an airplane and looking out the window. Typically, SAR sensors are configured to look either right or left. If the satellite is rotated, that direction can change. How an area is illuminated by a radar beam changes foremost with image acquisitions during ascending and descending overpasses of an area. **Figure 3.11** exemplifies the effect of look direction from ascending or descending data. The image subset is from the Sentinel-1 crossover pass in northeast Ecuador at the location shown in the right-hand part of the figure. The left side of the figure shows from top to bottom the combined layover and shadow masks from ascending and descending paths over a Google Earth subset. The center figure shows the descending path, and the bottom figure shows the ascending path. Differences in the backscatter can be seen as well as the varying locations of the layover and shadow masks (red color). Forest monitoring applications benefit from combining different look directions, as different regions will be mapped and complementary backscatter information can be retrieved.

Figure 3.12 shows an example of look direction effects for forest observations in Chile from L-band. The city of Talca lies in the western part of the images and can be seen as a rose-colored blob, similar another smaller city farther north. Note that in the ascending data, these two cities turn green in the multi-polarization L-HH/L-HV/ratio image to assume the same backscatter levels as the forests south of Talca and on the Andean slopes in the eastern part of the images. Incidence angle might also contribute with near- and far-range observations, although the gamma naught values mostly flatten the backscatter in the narrow ALOS-1 swath of about a 70-km swath width. Thus, here look direction is mostly causing a change in how the city and forests are seen structurally. Again, if time series analysis for change detection is targeted for forest monitoring, it is advisable to analyze time series by repeat-pass orbits and not mix ascending and descending datasets.

3.3.5 ROLE OF MOISTURE

SAR is very sensitive to moisture in soils and vegetation, and also to standing open water and below-canopy standing water. Increased moisture content in soils and vegetation tend to increase the backscatter signals. Standing open water has very dark image characteristics due to most of its energy being scattered in the forward direction away from the sensor; however, when wind, currents, or boat engines rough up water surfaces, strong backscatter can originate from open water surfaces. In particular, shorter wavelengths like C- and X-bands have strong open water surface backscatter from rough water surfaces. At longer wavelengths, the aforementioned double-bounce effect under canopies can have a strong backscatter signal (**Fig. 3.6**).

Figure 3.13 shows an example of moisture influence on the Sentinel-1 C-band data over Ecuador. The

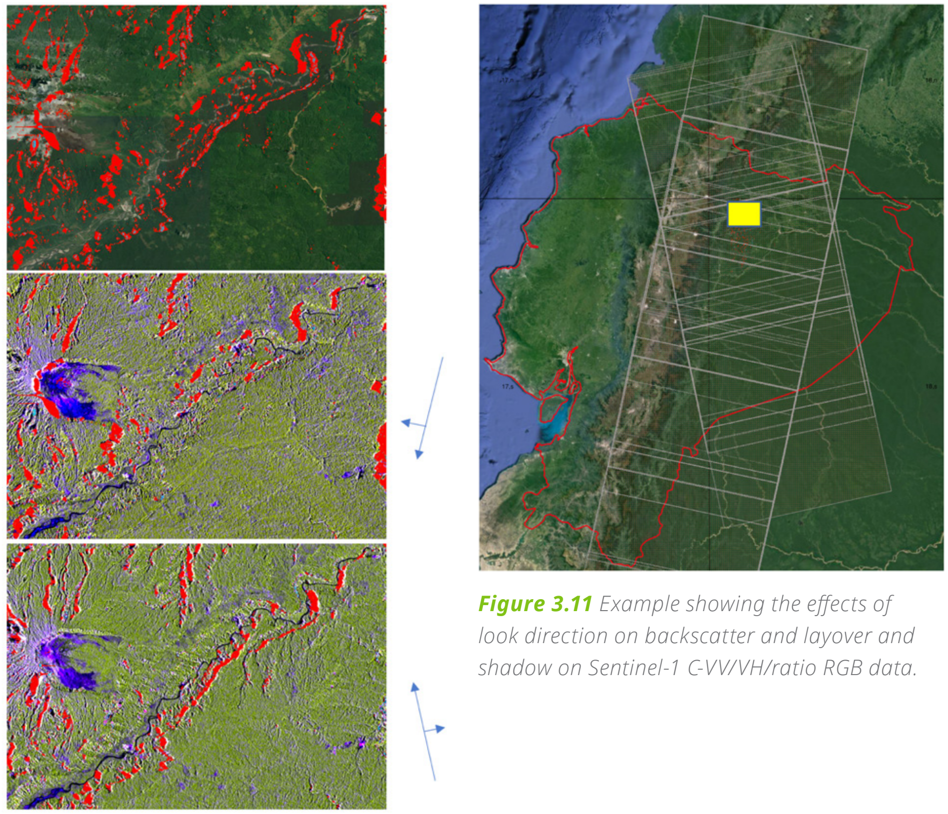

Figure 3.11 *Example showing the effects of look direction on backscatter and layover and shadow on Sentinel-1 C-VV/VH/ratio RGB data.*

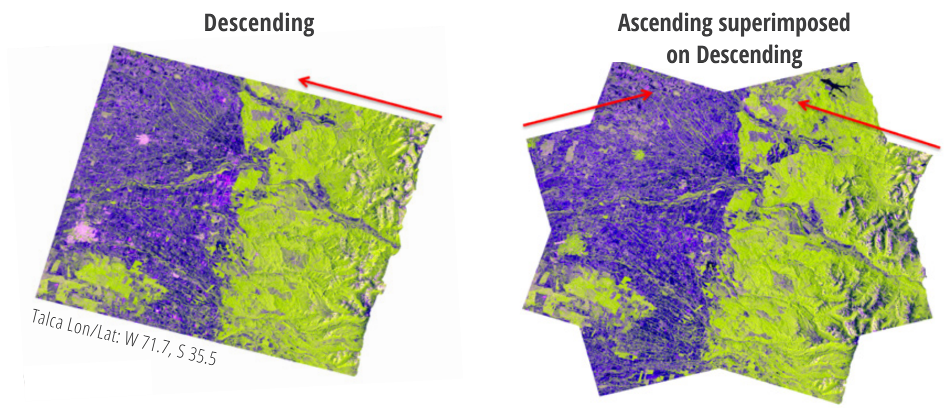

Figure 3.12 *ALOS-1 data over Chile, Talca, region from ascending and descending paths. RGB=L-HH/L-HV/ratio. Red arrows indicate the look direction of the right-looking sensor.*

darkening effects are associated with actively raining strong tropical convection systems that cause signal attenuation. The brightening effects stem from wet vegetation and soils from the rain events associated with the tropical frontal system. Riverbeds are still seen in the midst of brightened backscatter areas in the affected image from February 27, 2017, confirming that the SAR signals indeed stem from an increase in vegetation and soil moisture.

Figure 3.14 shows the effects of vegetation and soil moisture on signal brightening in L-band HH polarization from ALOS-1 at the Ecuador site. Three acquisitions from the end of June 2008, 2009, and 2010 are compared. While 2008 seems to have few effects

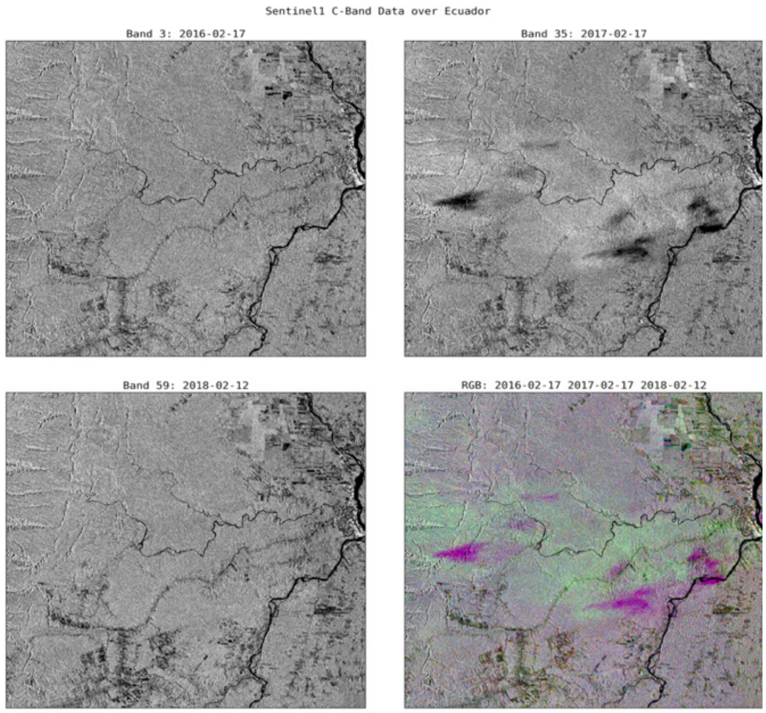

Figure 3.13 *Sentinel-1 CVV example of moisture influence on enhancing and darkening backscatter*

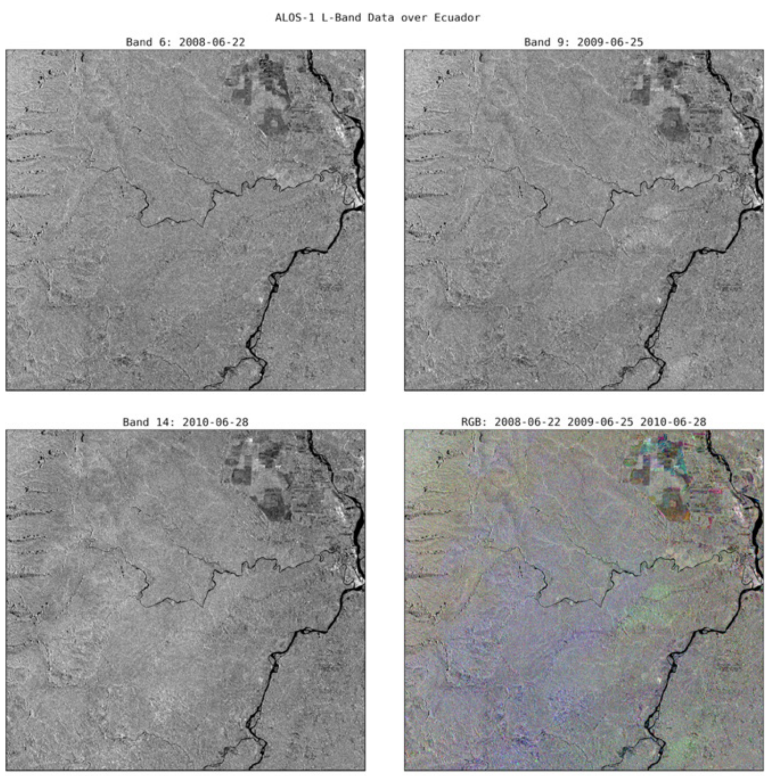

Figure 3.14 *ALOS-1 L-HH example of moisture influence on enhancing backscatter.*

from moisture-related backscatter enhancements, the year 2009 shows some effects in the eastern part of the image. In 2010, a strong moisture-related brightening is visible. As a result, the multitemporal color composite shows large-scale color variations that are moisture-related. Care must be taken when performing multitemporal image change detection for forest degradation so as to not to interpret darkening in a time series as a degradation signal when moisture variations can be the cause for decreases or increases in backscatter. Time series analysis can help to separate these effects, as moisture variations are shorter in time and space and exhibit a more random pattern compared to real disturbance or deforestation signals.

3.3.6 ROLE OF STRUCTURE

In addition to moisture conditions, vegetation structural characteristics determine SAR backscatter from forests. This includes both horizontal structure (i.e., canopy density, row plantations, texture) and vertical structure (i.e., crown depth, crown and trunk biomass, leaf and branching structure, life forms of trees, excurrent or decurrent growth). **Figure 3.15** provides a schematic overview of these structural classes (Dobson et al. 1996).

	Herbaceous		Woody			
Growth Form	Blade-like	Broadleaf	Shrubs	Trees		
				Excurrent	*Decurrent*	*Columnar*
					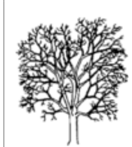	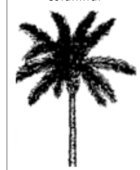
Structural Characteristics:	*(i.e. grass, corn)*	*(i.e. soybeans)*	*(i.e. alder)*	*Gymnosperms (i.e. pine)*	*Angiosperms Dicots (i.e. oak)*	*Angiosperms Monocots (i.e. palm)*
Trunks	None	None	Many small trunks with characteristic orientations	Conical trunk with layered dielectric	Cylindrical, forked trunk with layered dielectric	Cylindrical trunk of homogeneous dielectric
Branches	Non-woody stalks or stems	Non-woody stems	Many small branches & stems	Branch size/orientation varies with height; branches often long/thin	Forked branches, few horizontal elements; branches often short/thick	None
Foliage	Blade-like erectophile	Broad leaves	Blade-like or broad leaves	Needles	Broad leaves	Blade-like clump at top of trunk

Figure 3.15 *Description of simple structural classes of vegetation (Dobson et al. 1996).*

Figure 3.16 provides an example of backscatter response for C-VV and C-VH data for the oil palm plantation and its various growth, disturbance, and regrowth stages (including backscatter from undisturbed primary forest). The timing of the Google Earth subset corresponds to the C-band acquisition dates in September 2017.

For L-band sensors, **Figure 3.17** provides an example from a timber management area in Louisiana, U.S. The area is heavily managed, and various stages of clearcutting, selective logging (row thinning), and regrowth can be seen. The cross-polarized data clearly show increased brightness where there are more mature, higher biomass forests.

3.3.6 SUMMARY: DEFORESTATION AND FOREST DEGRADATION FROM A SAR POINT OF VIEW

In simple terms, broad characteristics of backscatter behavior can be summarized as follows:

- **Deforestation**—Predominantly a change from volume to surface scattering. This means cross-polarized (VH, HV) backscatter decreases significantly. However, if deforestation results in rough soil conditions (e.g., slash) or if site preparations rough up soils, backscatter can be significantly enhanced, to the point where actual felling events increase (e.g., until logs are removed). In time series observations, however, trends are towards reduced backscatter. Moisture conditions of soils that are more visible now can enhance signals at C-band significantly and can introduce ambiguities. Time series signals will reveal those transitions.
- **Degradation**—Degradation of forests typically reduces volume scattering and (depending on the amount of degradation) how much soil contributes to the backscatter signal at the observing wavelength. At C-band, degradation is tough to detect unless larger patches of forest are removed. L-band tends to have a detectable signal drop from forest thinning. However, the type of degradation also determines the scattering mechanisms. For example, storm damage may be such that vegetation volumes and scattering mechanisms have enhanced backscatter from slanted trunks, which is difficult to separate from before-disturbance signal strength. Fire events have a strong increase at L-band, where stronger soil contributions enhance double-bounce and hence brighten the backscatter signal. Over time, as volume starts to significantly degrade, the SAR signal follows a pattern of backscatter decrease in degraded forests.

Table 3.3 gives an overview of the expected backscatter characteristics for different vegetation transition scenarios.

3.4 Appropriate SAR Preprocessing Methods for Forest Applications

3.4.1 WELL-CALIBRATED, RADIOMETRICALLY TERRAIN CORRECTED SAR DATA

Proper RTC of SAR data is a crucial starting point for any analysis of change detection, either bitemporal, in time series, or in combination with optical datasets (see **Chapter 2** for RTC processing discussion). A word of caution: as of this writing, the open source software SNAP delivered by the European Space Agency (ESA) has two known shortcomings: (1) geolocation inaccuracies up to 40 m in the range direction and (2) radiometric correction that is suboptimal given the novel approach by Small et al. (2012). For change detection purposes, careful co-registration after processing with SNAP (i.e., with image matching postprocessing) might overcome some of these issues. However, it is important to assess whether backscatter change stems from geometric

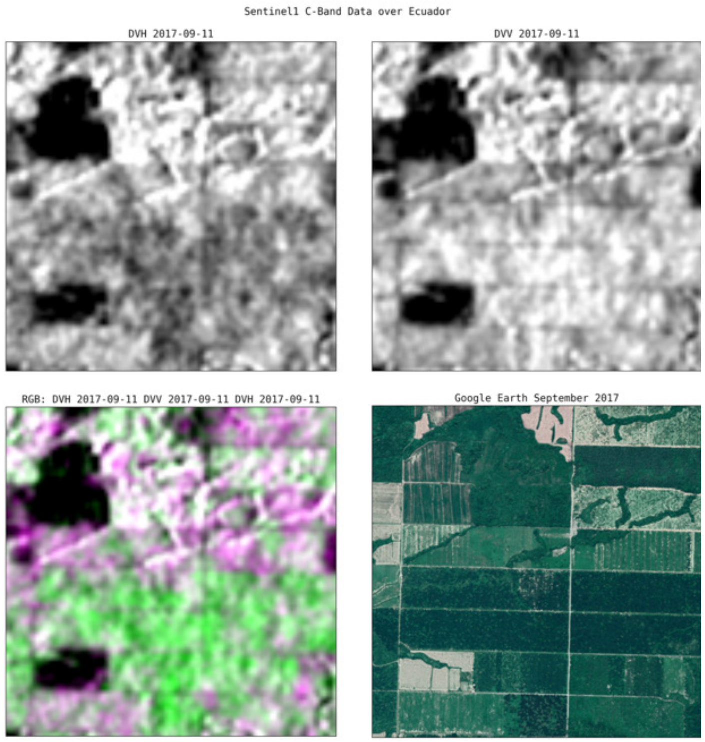

Figure 3.16 *Sentinel-1 C-band example of VV/VH backscatter in the oil palm plantation in Ecuador for different growth stages. Descending orbit (D).*

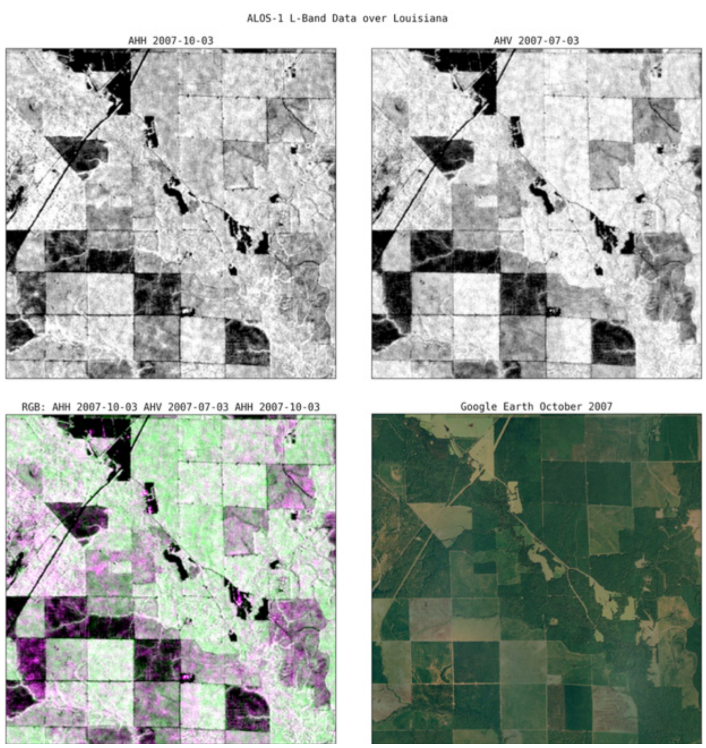

Figure 3.17 *ALOS-1 L-band data over a timber management region in southern Louisiana, U.S., showing various stages of clear cuts, selective logging, and regrowth. Ascending orbit (A).*

WAVELENGTH	POLARIZATION	RESPONSE BY FOREST TYPE					
		Sparse Forest (dry)	Sparse Forest (flooded)	Degraded Forest (dry)	Degraded Forest (flooded)	Dense Forest (dry)	Dense Forest (flooded)
C-band backscatter (g0)	VV	Medium to high; Depending on the roughness of the forest floor and moisture, there is lots of variation in this category	Low to medium; Depending on forest density, lots of forward scattering	Medium to high; most scattering from crown	Medium to high; most scattering from crown	Medium to high; most scattering from crown (Can be low in scenarios where absorption dominates and diminishes backscatter)	Medium to high; most scattering from crown (Can be low in scenarios where absorption dominates and diminishes backscatter)
	VH	Medium to high; Depending on the roughness of the forest floor and moisture, there is lots of variation in this category	Low to medium; Depending on forest density, lots of forward scattering	Medium to high; most scattering from crown	Medium to high; most scattering from crown	Medium to high; most scattering from crown (Can be low in scenarios where absorption dominates and diminishes backscatter)	Medium to high; most scattering from crown (Can be low in scenarios where absorption dominates and diminishes backscatter)
	VV/VH Ratio	Medium to high	Medium to high	Medium	Medium	Medium	Medium
L-band backscatter (g0)	HH	Low to medium; lower than dense forest and flooded sparse forest. At steep incidence angles, backscatter can be medium to high	Medium to high, depending on how much double bounce is contributing to the signal	Medium to high	High to very high, double bounce contributes to high backscatter	High to very high; higher than degraded forest, however at very high biomass levels we see saturation and no distinction with degraded forests	High to very high, double bounce contributes to high backscatter
	HV	Low to very low, depending on how dry the soils are	Low to very low. Most scattering is in the forward direction due to specular reflection	Medium to high	Medium to high, no seasonal variation with flooded forest floor	High to very high; volume scattering is dominant – best senstivity to biomass	Medium to high, no seasonal variation with flooded forest floor
	HH/HV Ratio	Medium	High	Medium	High	Medium	High

Table 3.3 *Expected backscatter characteristics for different vegetation transition scenarios. Note: Cross-polarized backscatter is generally lower than like polarized backscatter; backscatter values range from very low, low, medium, high, to very high.*

offsets rather than real change, particularly in hilly terrain. The quality of the DEM as an input to any orthorectification process is also critical. Note that SRTM-derived DEMs are often adequate for ~20- to 30-m resolution SAR processing; however, improvements in backscatter mapping could be achieved with better resolution DEMs. This is in some ways a question of cost/benefit ratios, as higher resolution DEMs are available, yet often not open source. All datasets shown in this chapter were produced with the Gamma Remote Sensing software, which is also employed by the Alaska SAR facility for RTC production and used by Earth Big Data, LLC, for all SAR geocoding. In preparation for the NISAR mission, the Jet Propulsion Laboratory (JPL) developed the InSAR Scientific Computing Environment (ICSE) software which will eventually be available to the community. A well-suited open source software for post-RTC processing is available in the Geospatial Data Abstraction Library (GDAL) packages from command line or as Python API bindings.

3.4.2 MULTITEMPORAL SPECKLE NOISE REDUCTION

If properly stacked SAR data are available (such as in a tiling scheme for manageable data volume handling), it is advisable to preprocess time series data stacks with a multitemporal speckle filter (e.g., by Quegan et al. 2001). Multitemporal speckle filters have been shown to preserve spatial detail while significantly reducing speckle noise at each time step. Multitemporal speckle filters estimate speckle characteristics along the time domain rather than the spatial domain. The resulting speckle statistics can be used to estimate a noise-reduced mean backscatter of a pixel, preserving the backscatter estimate at any time step, but at reduced noise. As such, spatial detail is preserved.

Figure 3.18 contains an example of L-band data from ALOS. Sixteen multitemporal scenes were available to reduce speckle noise using multitemporal speckle diversity. After filter application, various forest growth and logging states are much more discernible than before filter application. Given the color theory in **Section 3.2.2** and an understanding of volume backscatter changes in L-band HV for forests, the multitemporal image can be readily interpreted as to what areas underwent clearcutting or selective logging (red and yellow colors) and what areas are in regrowth (blue colors) or unchanged stage (white and black colors). Note that perfect alignment of pixels over the temporal domain is a prerequisite of successful multitemporal speckle filtering. Thus, it is advisable to apply the filter on data of the same repeat path.

3.4.3. A WORD ON POWER, AMPLITUDE, AND DB SCALES

With SAR data handling, it is important perform all spatial and temporal averaging operations in power scale. SAR data expressed in dB (logarithmic transformation) or amplitude scale (square root transformation) introduce mathematical errors when using these averaging or spatial convolution operations. This is also true for warping operations when convolutions on the SAR data are performed. Therefore, it is recommended that data be converted to the power domain during processing, such as the Earth Big Data's (EBD's) processing software for multitemporal filtering. The QGIS plugin of EBD's open source SAR time series visualization tool also uses power transformations behind the scenes when displaying time series in dB scale.

3.4.4 TILING AND CONSTRUCTION OF TIME SERIES FROM GEOTIFFS WITH VIRTUAL RASTER TABLES

With the advent of SAR sensors with global acquisitions at high temporal frequency, the era of time series analysis for SAR data has begun. Sentinel-1, with its two-sensor formation flights, now monitors most of the planet at 12-day repeat cycles, denser at higher latitudes. With swath width in high-resolution Interferometric Wide Swath mode at ~250 km, SAR data volumes become massive quite quickly. Thus, it is imperative that appropriate tiling schemes and data handling strategies are employed. For many reasons, the GeoTIFF image format has evolved as a standard for handling remote sensing imagery. In concert with the Virtual Raster Table (VRT) format from the GDAL library, GeoTIFFs can be very efficiently tied together into time series that can readily be subset or rearranged without the need for large raster data operations. VRTs are just XML-based headers that form the metadata for building image band stacks. But even more so, many raster operations can be prescribed as VRT processing in multiple steps, only to be executed on the data when the raster output is generated.

A tiling approach was developed for Sentinel-2 optical data at 20-m resolution based on the Military Grid Reference System (MGRS). This globally consistent Universal Transverse Mercator (UTM) projection-based approach keeps data consistent in spatial extent and projection across the globe. The pixel area of an MGRS UTM tile at the equator is the same as in a tile at higher latitudes. Arguably, this approach keeps data globally minimally distorted, and algorithms for spatial convolutions like speckle filters would work consistently on UTM data. This is not true for data in latitude/longitude spacing, where longitudinal pixel resolution changes with latitude. Using the Sentinel-2 MGRS tiling scheme also for Sentinel-1 data enables readily optical/SAR fusion without the need for further reprocessing. Hence, the EBD production suite readily provides Sentinel-1 SAR time series data stacks in MGRS tiling format.

A data guide explaining the naming conventions and tiling of VRT/GeoTIFF time series data stacks used by EBD products can be found here. GDAL can be used directly to build VRT stacks solely based in open source components.

BEFORE FILTER APPLICATION: **AFTER FILTER APPLICATION:**

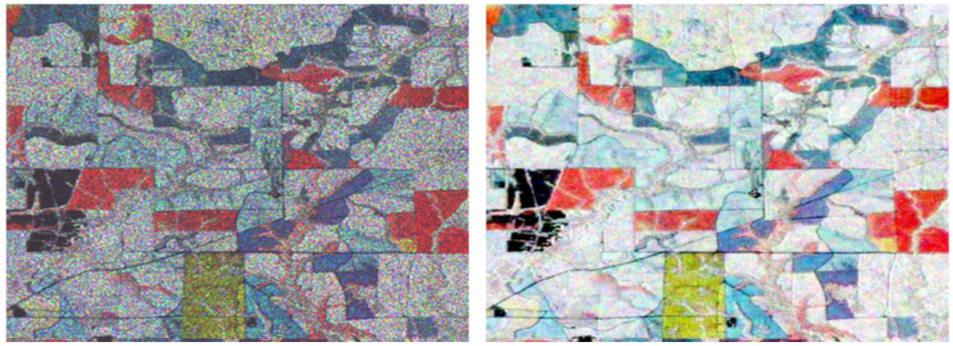

L-HV RGB: 2007-07-03 2009-07-08 2010-07-11

Figure 3.18 *Multitemporal speckle filter application on a perfectly co-registered time series data stack of ALOS L-band data over Louisiana, U.S*

3.5 Change Detection Approaches for SAR Data

3.5.1 BITEMPORAL METHODS

Classic image change detection methods for bitemporal image comparison can be applied to well-calibrated RTC SAR imagery. The log-ratio method was explained in **Chapter 2**. The Iteratively reweighted Multivariate Alteration Detection (iMAD) algorithm (Nielsen 2007) holds promise for change detection between two images; however, as shown in previous sections, it is important to understand possible impacts on backscatter change that are not linked to real changes such as deforestation. While forest changes are easier to detect in bitemporal analyses at L-band, C-band data often present a challenge, as surface roughness and moisture components can lead to significant SAR signal ambiguities.

3.5.2 TIME SERIES ANALYSIS METHODS

In the past, the availability of SAR data was sparse in space and time; however, the Sentinel-1 mission has been a game changer in moving SAR into operational use. The upcoming NISAR mission—with its open data policy and L-band data at 12-day repeat intervals at medium resolution—will be the next big push for SAR data availability. With near-continuous availability of SAR observations of the ground, real time forest monitoring can thus be achieved. Time series analysis techniques developed for optical imagery are somewhat applicable, although SAR characteristics of backscatter sensitivity to structure and moisture warrant a closer look at new methods. Change point detection with cumulative sums (Manogaran & Lopez 2018) is an established time series analysis technique stemming from the financial sector. With the general SAR backscatter trending to decrease with biomass loss due to deforestation or forest degradation, the application of cumulative sum analysis to SAR time series data seems potentially simple, yet powerful.

The following figures show time series signals over a deforestation event in Ecuador observed

__Figure 3.19__ Ecuador logging test site

with Sentinel-1 data from 2016 to 2018 that exemplify the strength of SAR time series for forest change detection. **Figure 3.19** shows a 4-x-4-km^2 subset of an active logging region in the northeastern part of Ecuador, and **Figure 3.20** shows the time series profile and associated imagery for a logging event in January 2017. While some noise exists in the time series, a clear backscatter decrease in early 2017 is visible in the center image and time series plot. As is typical for deforested areas at C-band, lower backscatter at higher variability is observed in the C-band profile after the deforestation event. This disturbance observation can be identified from the longer trends visible compared to more short-term random noise due to moisture variations. After applying a kernel filter to smooth the time series somewhat, a cumulative sum curve can be constructed from the residuals of the time series data, minus the mean observation of the entire time series.

Figure 3.21(a) shows the smoothed time series profile and the mean of the time series used to calculate the residuals. The cumulative sum of the residuals is shown as the peaking blue curve in the bottom panel. A way to establish the validity and significance of a candidate change point is to perform a bootstrap analysis in which the time steps are randomly reordered and cumulative sums of the randomized residuals are computed. If the randomization ($n > 500$) shows few or no

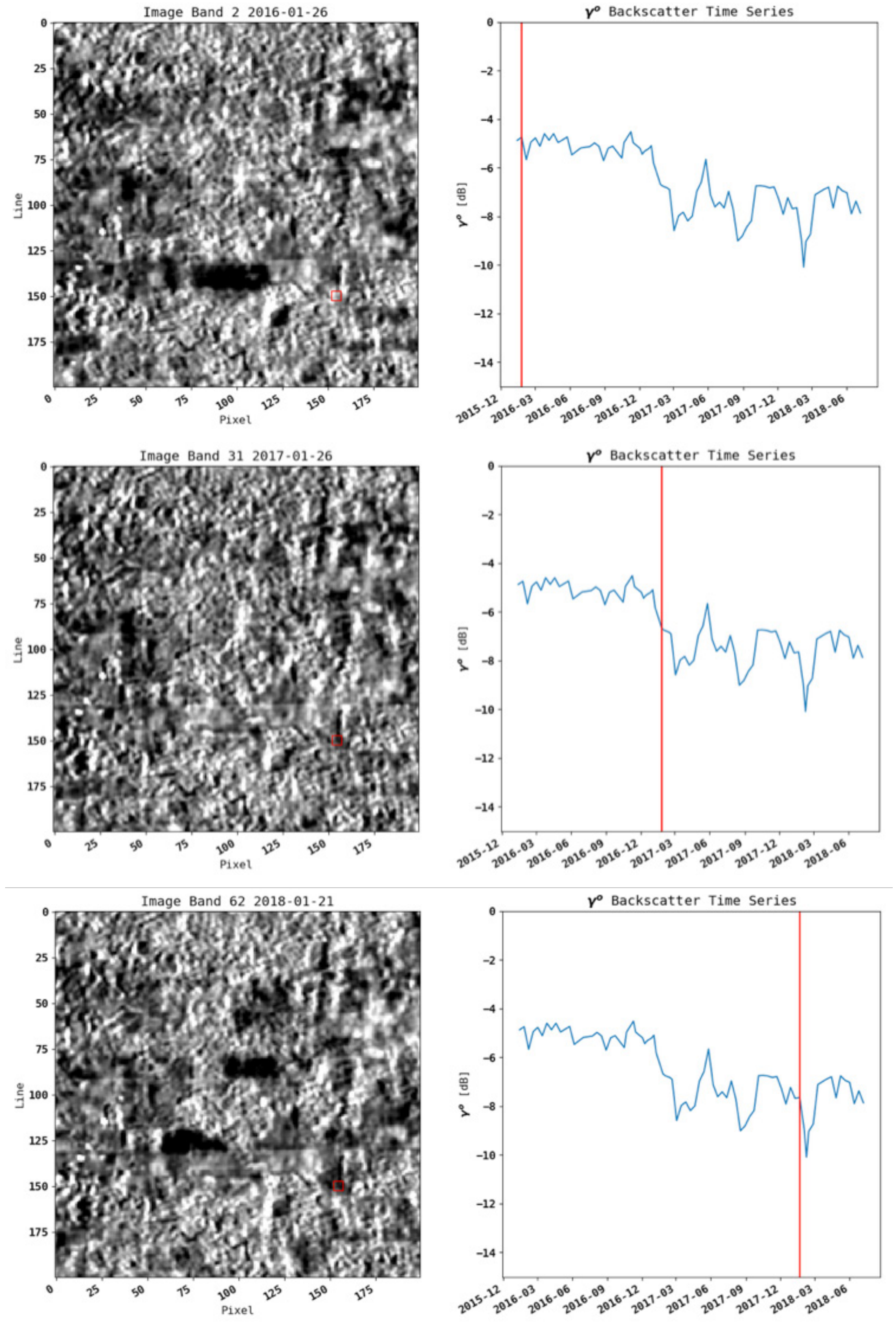

__Figure 3.20__ Time series profile of red square with associated Sentinel-1 descending VV data.

curves reaching the same maximum value of the peak of the cumulative sum curve (which is the change point in time) the point can be labeled valid. The bootstrapping thus provides a confidence level for a detected change point. Other metrics can aid in the confirmation of change points in a SAR time series, as elaborated with formulas and Python code in the training Jupyter Notebooks that go along with this chapter. As can be seen in **Figure 3.21(b)**, the 500-fold randomization shows

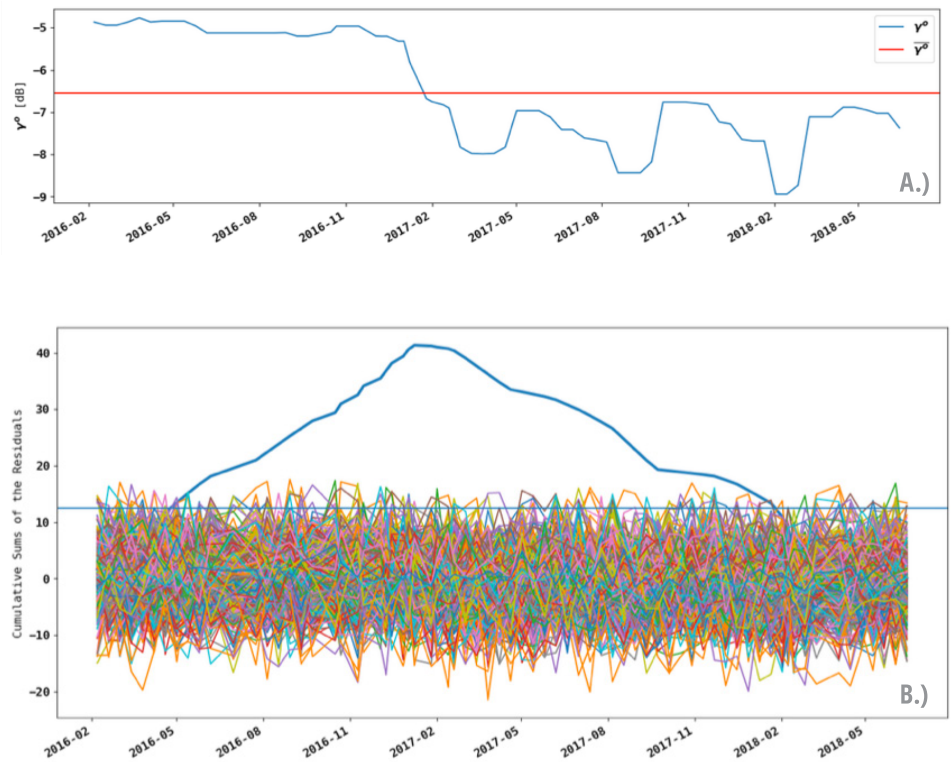

Figure 3.21 *(a) Smoothed time series and mean backscatter, and (b) 500 cumulative sums of the residuals of the time series, minus the mean and 500-fold bootstrapped cumulative sum curves.*

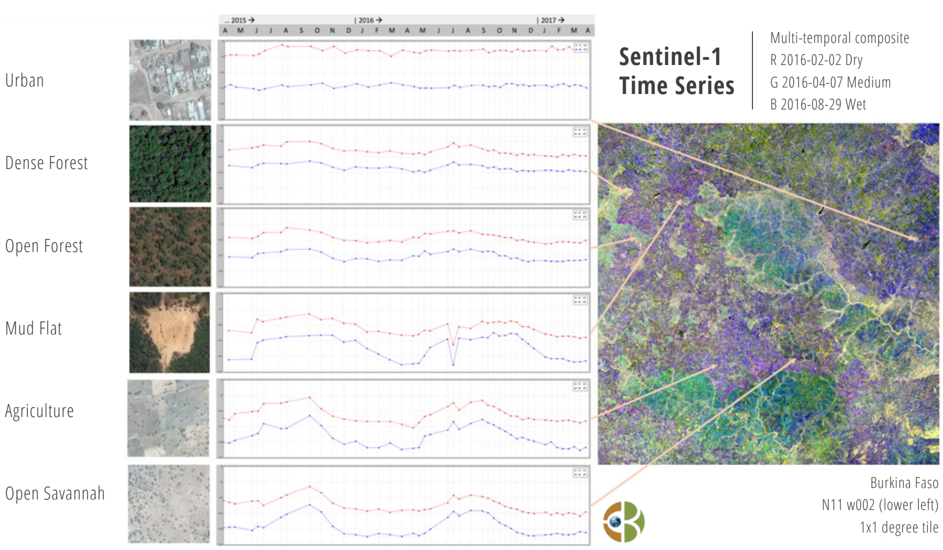

Figure 3.22 *Sentinel-1 time series profiles of forest and non-forest land cover patches. Red profiles are C-VV, and blue profiles are C-VH backscatter curves. The backscatter range in each subset shows backscatter from 0 to −20 dB for the SAR g^0 values. The timeframe covers dates from April 2015 to April 2017.*

that all randomized S-curves are significantly lower in their peak values compared to the candidate change point in the observed time series.

Applying this approach to all pixels in the subset results in the identification of change pixels and the detected dates of change shown in **Figure 3.22** (right panel). The color codes correspond to the change dates, at a time resolution of about 12 days. The left panel in this figure shows a multitemporal color composite of Sentinel-1 descending VV acquisitions from 2016-11-15 (red), 2017-08-29 (green), and 2018-05-21 (blue). Note that many of the red and yellow color tones in this multitemporal composite correspond to the expected and detected deforestation and forest degradation events. However, some red tones also are more associated with changes in agricultural patterns, which were correctly not mapped as forest degradation events, as their time series profiles did not match the type of curves seen in the previous profiles.

Lastly, to confirm the capability of Sentinel-1 SAR time series to map logging progression, a close-up of the earliest detected event in this region is shown in **Figure 3.23**. Change dates show the progression of the logging of a 5-ha area over the course of four months starting in the southeast corner of the patch and progressing to the west.

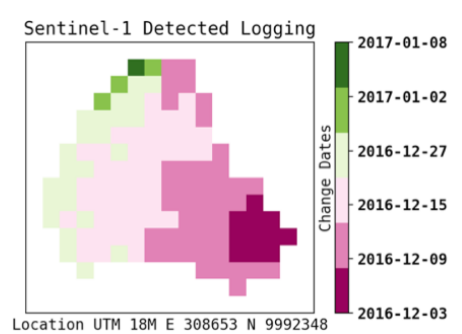

Figure 3.23 *Logging progression detected from Sentinel-1 satellites. A 20-m pixel spacing the subset covers 300 x 320 m2. The logged area is 5 ha.*

3.5.3 SUMMARY ON TIME SERIES SIGNAL ANALYSIS FOR SAR BACKSCATTER DATA

In summary, SAR time series data, such as those now available from Sentinel-1, are an invaluable resource for detailed forest change mapping with quasi-continuous mapping capacity from the sensors. Note that several regions of the planet might be covered more often with ascending or descending data, single-polarization VV or dual-polarization VV+VH datasets. The upcoming NISAR mission will bring the same datasets and temporal frequency at L-band, which will increase forest change detection capability, as fewer signal ambiguities in the time series exist with clear drops in backscatter from deforestation and forest degradation activities.

An example of a semi-arid region and time series signal variation at C-band is provided for Burkina Faso. **Figure 3.22** exemplifies the moisture and structure dependency of various dense forests. Note in this figure how backscatter varies by season due to an increase in moisture and agricultural activity. Even a strong rain event seems to be detected in April 2016, leading to a spike in almost all curves but urban and the mud flat. The mud flat profile shows a strong drop at one date (which is most likely associated with a flash flood event from the heavy rain event), leading to open water surface detection in the time series. Also note that the amplitude in the time series signal increases with decreasing canopy cover, which can be attributed to an increase in soil moisture signal contribution during the rainy season. It can be seen that with decreasing density, the seasonal moisture changes contribute to the rise and fall of backscatter. Thus, it is again important to keep in mind that backscatter signals vary over time, which is vital for careful selection of seasons for time series analysis. A compilation by Ulaby et al. (2014) entitled *Microwave Radar and Radiometric Remote Sensing* contains in-depth resources for SAR data backscatter behavior from soil and vegetation targets.

3.5.4 OPTICAL/SAR FUSION FOR FOREST MAPPING

SAR and optical data provide complementary information for forest monitoring, as different imaging principles underlie the SAR backscatter and optical multispectral reflectance measurements. As previously noted, SAR measures changes in vegetation and soil moisture content as well as the structural composition of the vegetation (lifeforms). Optical remote sensing measures changes in the chemical composition of leaves and their reflectance when illuminated by sunlight, also including measurements of shadow fractions within canopies. Indices like the Normalized Difference Vegetation Index (NDVI) (Tucker 1979) normalize optical reflectance values and provide a measure of the vegetation density or leafiness. Thus, studies of SAR backscatter and NDVI can be used to compare time series of optical and SAR data. Several studies have exploited these similarities, fusing SAR data from Sentinel-1 and ALOS and Landsat time series (Reiche et al. 2016). Various approaches for fusing time series data can be applied. Attempts have been made to fuse time series at the *signal level*, where optical and SAR signals are normalized to simulate similar trends in a fused time series (e.g., filling NDVI gaps with simulated SAR backscatter assuming similar behaviors). This is problematic, however, given that the signals have different underlying principles, although some successes have been demonstrated (Reiche et al. 2015).

Another approach is fusion at the *prediction level*, that is, optical and SAR time series are analyzed separately, and probabilities for deforestation and forest degradation events are computed and compared in the time domain. This has an advantage in that inherent sensor characteristics are optimally analyzed, and probabilities as dimensionless measures can readily be fused in a time series. As such, SAR can fill time gaps in optical observations, and joint probabilities can confirm detections from separate optical or SAR analyses. Holden et al. (forthcoming) developed and tested two approaches for fusing time series of Landsat reflectance and L-band backscatter time series for mapping deforestation for a site with both small- and large-scale agroforestry near Yurimaguas, Peru. This "Probability Fusion" approach—similar to the approaches used by Reiche et al. (2015, 2018)—performed slightly better for finding deforestation with radar data in terms of map accuracy (78.9% vs. 75.6%) and change detection timing, even with a relative abundance of Landsat data and only 11 radar observations. The improvement when using radar data was much higher when simulating reductions to Landsat data availability. Their "Residual Fusion" algorithm relies on time series regression forecasts (similar to BFAST Monitor (Verbesselt et al. 2010) or CCDC (Zhu et al. 2012)) and was less accurate when fusing data sources than when using Landsat alone, likely because there were too few radar observations to reliably develop forecast regression models. The authors encourage further development of time series fusion algorithms that can incorporate data from current and upcoming radar missions, especially approaches that can go beyond just deforestation mapping to provide class transition labels for IPCC reporting.

3.6 Conclusions

With the launch of Sentinel-1 and its associated open data distribution, monitoring forest resources at medium resolution with SAR has now reached operational levels. The C-band mission of the Sentinel-1 sensors are already projected to 2030 in ESA's budget. NASA and ISRO are poised to launch the L-band NISAR missions at the beginning of the next decade, which will provide 12-day repeat global L-band and regional S-band acquisitions, also with an open data policy. As shown in this chapter, SAR data have a strong sensitivity to forest change. Careful preprocessing is required to build good time series data stacks. Seasonal and moisture variations need to be separated from structural changes in change detection approaches. This requires potentially filtering of the time series to remove "outliers." Cumulative sum-based change detection of SAR backscatter mean shifts are amongst efficient change detection techniques of the continuously available time series signals.

3.7 References

Craig Dobson, M., Pierce, L. E., & Ulaby, F. T. (1996). Knowledge-Based Land-Cover Classification Using ERS-I/JERS-1 SAR Composites. IEEE Transactions on Geoscience and Remote Sensing, 34(1). http://doi.org/10.1109/36.481896

Henderson F., Lewis A. (Eds.) (1998). Principles and Applications of Imaging Radar. Manual of Remote Sensing, 3rd Edition, Volume 2, John Wiley and Sons.

Holden, C., Woodcock, C., Kellndorfer, J. (Forthcoming). Forest change detection by radar/optical time series fusion: a comparison of two approaches using Landsat and ALOS PALSAR.

Kelldorfer, J. M., & McDonald, K. C. (2008). Active and Passive Microwave Systems. In The SAGE Handbook of Remote Sensing. http://doi.org/10.4135/9780857021052.n13

Kellndorfer, J., Cartus, O., Bishop, J., Walker, W., & Holecz, F. (2014). Large Scale Mapping of Forests and Land Cover with Synthetic Aperture Radar Data. In Land Applications of Radar Remote Sensing. http://doi.org/10.5772/58220

Manogaran, G., & Lopez, D. (2018). Spatial cumulative sum algorithm with big data analytics for climate change detection. Computers and Electrical Engineering, 65, 207–221. http://doi.org/10.1016/j.compeleceng.2017.04.006

Mitchell, A. L., Rosenqvist, A., & Mora, B. (2017). Current remote sensing approaches to monitoring forest degradation in support of countries measurement, reporting and verification (MRV) systems for REDD+. Carbon Balance and Management, 12(1), 9. http://doi.org/10.1186/s13021-017-0078-9

Nielsen, A. A. (2007). The regularized iteratively reweighted MAD method for change detection in multi- and hyperspectral data. IEEE Transactions on Image Processing, 16(2), 463–478. http://doi.org/10.1109/TIP.2006.888195

Quegan, S. (2001). Filtering of multichannel SAR images. IEEE Transactions on Geoscience and Remote Sensing, 39(11), 2373–2379. http://doi.org/10.1109/36.964973

Reiche, J., Verbesselt, J., Hoekman, D., & Herold, M. (2015). Fusing Landsat and SAR time series to detect deforestation in the tropics. Remote Sensing of Environment, 156, 276–293. http://doi.org/https://doi.org/10.1016/j.rse.2014.10.001

Reiche, J., de Bruin, S., Hoekman, D., Verbesselt, J., Kellndorfer, J., Rosenqvist, A., Lehmann, E., Woodcock, C., Seifert, F., Herold, M. (2016). Combining satellite data for better tropical forest monitoring. Nature Climate Change, 6, 120-122.

Reiche, J., Hamunyela, E., Verbesselt, J., Hoekman, D., & Herold, M. (2018). Improving near-real time deforestation monitoring in tropical dry forests by combining dense Sentinel-1 time series with Landsat and ALOS-2 PALSAR-2. Remote Sensing of Environment, 204, 147–161. http://doi.org/https://doi.org/10.1016/j.rse.2017.10.034

Small, D. (2011). Flattening Gamma: Radiometric Terrain Correction for SAR Imagery. IEEE Transactions on Geoscience and Remote Sensing, 49(8), 3081–3093. http://doi.org/10.1109/TGRS.2011.2120616

Tucker, C. J. (1979). Red and photographic infrared linear combinations for monitoring vegetation. Remote Sensing of Environment, 8(2), 127-150. http://doi.org/10.1016/0034-4257(79)90013-0

Ulaby, F. T., Moore, R. K., & Fung, A. K. (1986). Microwave remote sensing: active and passive. From theory to applications (Vol. 3). Reading, MA: Addison-Wesley.

Ulaby, F. T., & Dobson, M. C. (1989). Handbook of radar scattering statistics for terrain. The Artech House remote sensing library. Norwood, MA: Artech House.

Ulaby, F. T., & Elachi, C. (1990). Radar polarimetry for geoscience applications. Norwood, MA: Artech House.

Ulaby, F. T., D. G. Long, W. Blackwell, C. Elachi, A. Fung, C. Ruf, K. Sarabandi, J. van Zyl, and H. Zebker (2014), Microwave Radar and Radiometric Remote Sensing, 1116 pp., Artech House, Norwood, Mass.

Verbesselt, J., Hyndman, R., Newnham, G., & Culvenor, D. (2010). Detecting trend and seasonal changes in satellite image time series. Remote Sensing of Environment, 114(1), 106–15. http://doi.org/10.1016/j.rse.2009.08.014

Woodhouse, I. (2006). Introduction to Microwave Remote Sensing. Boca Raton: CRC Press.

Zhu, Z., Woodcock, C. E., & Olofsson, P. (2012). Continuous monitoring of forest disturbance using all available Landsat imagery. Remote Sensing of Environment, 122, 75–91. http://doi.org/10.1016/j.rse.2011.10.030

DR. JOSEF KELLNDORFER'S research focuses on monitoring and assessing terrestrial and aquatic ecosystems, and disseminating Earth observation data products to policy makers to improve decision making and support capacity building. He is a distinguished visiting scientist at the Woods Hole Research Center and currently serves on various expert working groups within NASA, the Japanese Space Agency JAXA, the Group on Earth Observation, and GOFC-GOLD to advance the use of remote-sensing technology for natural resource mapping and monitoring. He is a member of the NASA Science Team for the US/Indian NISAR satellite. He founded Earth Big Data to provide scalable solutions to modern data-mining challenges.

Writing this chapter and development of the training material was supported by the NASA SERVIR program. Sentinel-1 and ALOS examples were based on data from the Alaska Satellite Facility and work over many years with the JAXA Kyoto and Carbon Science Team. The following NASA grants supported some analysis of this work: NASA Carbon Monitoring System program, grant number 80NSSC18K0190; NASA NISAR Science Team, grant number 80NSSC18K0087.

Kellndorfer, Josef. "Using SAR Data for Mapping Deforestation and Forest Degradation." SAR Handbook: Comprehensive Methodologies for Forest Monitoring and Biomass Estimation. Eds. Flores, A., Herndon, K., Thapa, R., Cherrington, E. NASA. 2019. DOI: . 10.25966/68c9-gw82